PERGAMON

Journal of Structural Geology 25 (2003) 1487–1506

JOURNAL OF STRUCTURAL GEOLOGY

www.elsevier.com/locate/jsg

3-D stochastic modeling and simulation of fault zones in the Albalá granitic pluton, SW Iberian Variscan Massif

J. Escuder Viruete[a,*], R. Carbonell[b], D. Martí[b], A. Pérez-Estaún[b]

[a]*Depto. Petrología y Geoquímica, Universidad Complutense. E-28040 Madrid, Spain*
[b]*Inst. Ciencias de la Tierra Jaume Almera-CSIC. Lluís Solé i Sabarís s/n. E-08028 Barcelona, Spain*

Received 31 October 2001; received in revised form 7 August 2002; accepted 18 October 2002

Abstract

A distribution of fracture index (FI) is obtained from stochastic modeling and simulation to characterize quantitatively the fault system of the Mina Ratones area in three-dimensions (3-D). FI is a quantitative estimate of the fracture intensity in discrete domains of the granitic rock massif. The resulting 3-D grids, expressed as block (cells) models or contoured isosurfaces of FI, show high and low FI zones. The correlation of these zones with mapped faults allows two structural domains to be distinguished: (1) variably irregular surfaces of high FI, and (2) rhomboidal blocks of low FI located inside them. High FI domains (FI $> 4.2\ m^{-1}$) are interpreted as fault zones, since there is a good correlation at the surface between the domains and traces of the major fault zones. Low FI blocks (FI $< 2.5\ m^{-1}$) correspond to less fractured granite. The contact between high and low FI domains is gradual. The high and low FI structural domains may correspond with the damage zone/fault core and the protolith in the model for fault zone architecture of Caine et al. (1996). Therefore, 3-D grids of the FI in granitic areas affected by strike-slip brittle tectonics, such as Mina Ratones, constitute an image of fault zone architecture.

Keywords: Stochastic modeling; Fault zones; Granitic rock massif; Fracture index distribution method; Iberian Variscan Massif

1. Introduction

Brittle fault zones are lithologically heterogeneous and structurally anisotropic discontinuities in the upper crust (Caine et al., 1996). Following a conceptual model of fault zone architecture, faults can be divided into two distinct zones: the fault core, where most of the displacement is accommodated, and the damaged zone, which is mechanically related to the growth of the fault zone (Chester and Logan, 1986, 1987; Smith et al., 1990; Forster and Evans, 1991; Caine et al., 1993, 1996; Scholz and Anders, 1994). Fault core materials are commonly composed of one or more structural and lithologic elements such as anastomosing slip surfaces, clay-rich gouge, cataclasite and fault breccias. Damage zone structures are mechanically related fracture sets, small faults, veins and joints. The fault core and damage zone are surrounded by relatively undeformed protolith. The relative shapes and sizes of each of these structural components will vary from fault to fault and within a fault system and there may be more than one fault core or principal slip surface within a fault zone (Chester and Logan, 1987; Chester et al., 1993; Evans and Chester, 1995; Schulz and Evans, 1998, 2000). From a lithologic, structural and hydrogeological point of view, fault core, damage zone and undeformed protolith are distinct units that reflect the material properties and deformation conditions within a fault zone (Caine et al., 1996; Schulz and Evans, 1998, 2000). This architecture controls the physical properties of fault zones that include porosity, permeability, fluid flow, their mechanical behavior and geophysical signatures.

However, insufficient data, particularly field-based data, are normally available to adequately characterize the amount and distribution of each component of fault zones, especially in three dimensions (3-D) (Caine et al., 1996). The difficulty of measuring in situ fault zone properties increases in areas where outcrops are not continuous, nor homogeneously distributed. Consequently, adequate characterization of the spatial and temporal variations in fault zone permeability, porosity, fluid flow and other

* Corresponding author.
E-mail address: escuder@eucmax.sim.ucm.es (J. Escuder Viruete).

0191-8141/03/$ - see front matter © 2003 Elsevier Science Ltd. All rights reserved.
PII: S0191-8141(02)00183-9

geochemical and geophysical properties is frequently hindered.

Because of the difficulty of characterizing fault zone architecture, the assumption of structural homogeneity in the rock massif is commonly assumed. For example, in most fluid flow models for crystalline rocks analytical solutions are used to facilitate simplicity (e.g. equivalent porous media models), and because they have served well in illustrating basic concepts of mass transfer by advection and diffusion. While the influence of heterogeneous fault zones on permeability, fluid flow, chemical changes and fluid-flow interactions in crystalline massifs has been recognized (Barton et al., 1988; Scholz and Anders, 1994; Goddard and Evans, 1995; Caine et al., 1996; Schulz and Evans, 1998, 2000), these studies have treated each physical property (e.g. permeability) as a parameter of individual geological units, and each unit has been assigned a constant value (exception being Lopez and Smith (1996)). As an alternative to this type of deterministic modeling, in this study we present a geostatistical approach to describe spatially heterogeneous fault zones in a granitic massif, located in the Mina Ratones area of the SW Variscan Iberian Massif. This analysis was pioneered in mining, petroleum engineering and in hydrogeology because it permits a statistical or probabilistic description of the spatial variability inherent in natural systems.

2. Stochastic modeling of fault zones in granitic massifs

2.1. Fracture intensity

A common observation in many fault zones is that fracture intensity in the damage zone increases toward the central fault core yielding a fracture density gradient (Hancock, 1985; Goddard and Evans, 1995; Caine et al., 1996; Schulz and Evans, 1998, 2000). This fracture intensity can be quantitatively defined by a fracture index (FI), or number of structural discontinuities measured by unit length of scanline in outcrop or drill cores (m^{-1} units; La Pointe and Hudson, 1985; Narr and Suppe, 1991; Engelder et al., 1997). Based on the presence of a fracture density gradient perpendicular to a fault zone, FI estimates in discrete domains can be used to characterize fault zone architecture and its spatial variability using geostatistical methods. For example, Escuder Viruete et al. (2001) describe that relatively high FI values measured in outcrops are often adjacent to other relatively high FI areas, while low FI values cluster next to each other. High FI areas correspond with zones where fractures cluster next to each other, typical of fault damage zones. In the area studied by these authors, these high FI areas are two-dimensional (2-D) elongated bands parallel and coincident to the traces of mapped faults.

FI is not only likely to be elevated in a damage zone, but also to be highly variable in detail (Schulz and Evans, 1998, 2000). However, as shown in the conceptual model of Fig. 1, if the damage zone-fault core of the elongated fault zones and the surrounding undeformed protolith are divided into many small individual cubes, the average FI of each cube would be correlated with its surrounding cubes. The closer two cubes are to each other, the higher the probability that the FI values are similar. One aim of geostatistics is to describe this kind of spatial correlation to allow for prediction of non-measured values. Geostatistics assumes that natural variations can be described by a random, spatially correlated function. By making this assumption, a geostatistical approach is able to avoid the difficult task of reconstructing the exact processes that influenced the parameter value at each location.

2.2. Variograms and geostatistical simulation

A semi-variogram function (Isaaks and Srivastava, 1989; Deutsch and Journel, 1992; Cassiraga and Gómez Hernández, 1996; Pannatier, 1996; Fig. 2) is used to illustrate the behavior described above. For a set of n spatially distributed measurements of a property (z), the semi-variogram considers all N pairs of measurements (z_i, z_{i+h}) separated from each other by a distance h. The semi-variogram value $\gamma(h)$, for a separation distance h, is calculated by the sum over all $[z_i - z_{i+h}]$ pairs located at distance h from each other:

$$\gamma(h) = [1/2N(h)]\Sigma_{i=1\ldots N(h)}[z_i - z_{i+h}]^2 \quad (1)$$

The sample variogram is obtained by plotting all the intervals of class h versus the value of the semivariance $\gamma(h)$ calculated in each interval (Isaaks and Srivastava, 1989; Journel, 1989). If a spatial correlation exists between the data, typical variograms are convex curves where it is possible to extract several parameters that define the spatial continuity model of the property (Fig. 2), following the methodology described below (Isaaks and Srivastava, 1989; Deutsch and Journel, 1992; Cassiraga and Gómez Hernández, 1996; Pannatier, 1996). The spatial continuity can be used to estimate the values of the property in points, cells or blocks, in one, two or three-dimensions (1-, 2- or 3-D).

If the statistical characteristics of a geological unit are known from a set of spatially distributed data, unknown values for unmeasured points can be inferred so that the estimated unknown values also reproduce the unit's statistical characteristics. In granitic rocks, for example, where in situ fracture density cannot be fully determined in 3-D, inferences about fault zone architecture cannot be made directly. Instead, numerical simulations allow for the synthesis of FI stochastic fields with specified statistical characteristics. The numerical synthesis of stochastic fields requires specification of the mean, standard deviation, variance and spatial correlation of the data (variogram function). Currently, it is assumed that these properties do not vary with time. The manner of change of the variogram function with direction and increasing distance is specified

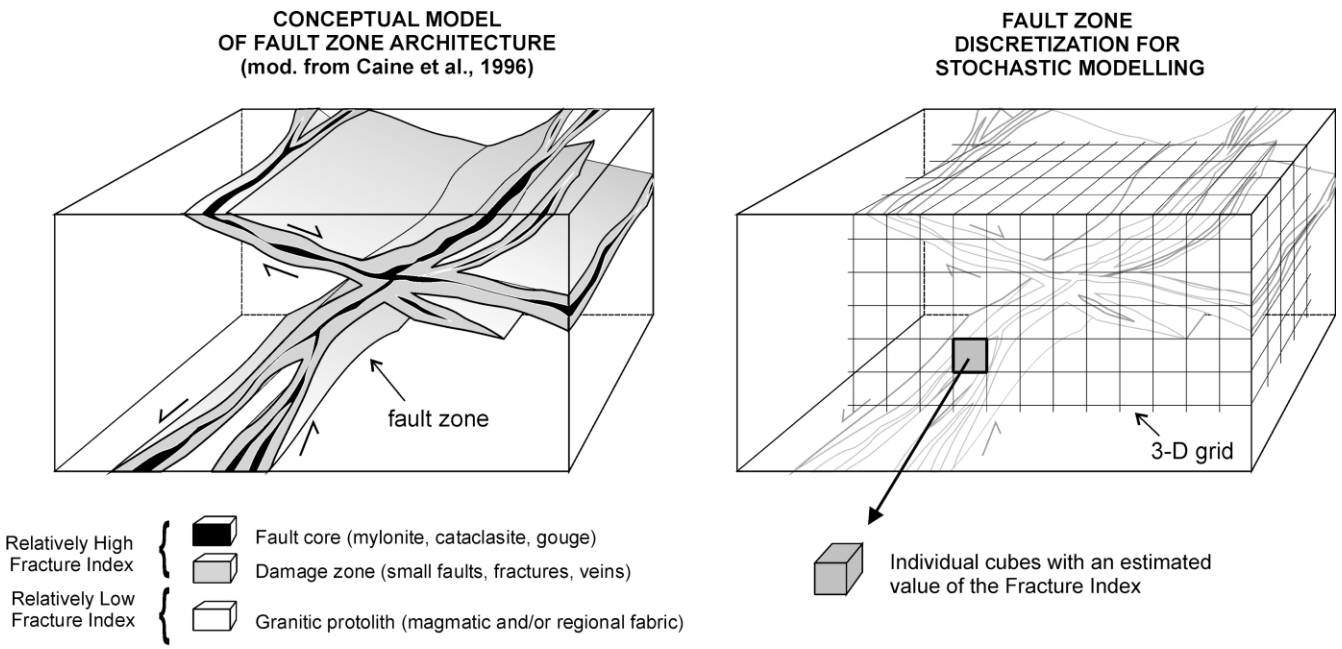

Fig. 1. Schematic illustration of the principal of spatial correlation used in stochastical modeling. (a) Conceptual model of fault zone architecture with protolith removed (after Smith et al., 1990; Caine et al., 1996). (b) Granitic massif discretization in small volumes (3-D grid) with a given value of the fracture index (FI) from geostatistical modeling. Each cube chosen from the damage zone-fault core is more likely to have high FI. Individual values of FI will thus be spatially correlated with neighbors. For a complete stochastic description of the FI distribution in 3-D, a correlation length is needed as well as the average FI of the granitic rock massif.

by selecting an anisotropic variogram model. These stochastic fracture intensity fields can be used in mass-transport models or in building physical property fields related to fault zones, and the resulting numerical predictions about structural, geochemical or mineralogical distributions can be compared with field-based observations.

The main objective of this work is to test if the FI distribution obtained from variogram modeling and geostatistical simulation in the Mina Ratones area quantitatively characterizes the fracture system in 3-D. In this case, geostatistical data are georeferenced FI values, measured at known locations in the 3-D granitic massif. Geostatistical modeling of FI involves the estimation of the spatial correlation described in the sample variograms and fitting a theoretical model to them (Englund and Sparks, 1991; Deutsch and Journel, 1992; Pannatier, 1996). Geostatistical simulations (or stochastic representations) can be seen as possible realizations of a spatially correlated random field, they all honour the spatial moments (mean, variogram) of the field (Gómez Hernández and Srivastava, 1989; Deutsch and Journel, 1992; Gómez Hernández and Cassiraga, 1994; Cassiraga and Gómez Hernández, 1996). Different simulations may be completely independent, only sharing the spatial moments (unconditional simulation) or they may in addition reproduce a set of observed values (conditional simulation). Showing multiple simulations can help the understanding of the combined effect of prediction uncertainty and spatial variation of the underlying process.

The results of the 3-D stochastic modeling and simulation of FI provide an image of fault zone architecture in the granitic rock massif. As an explicit assessment of the quality and limitations of geostatistical analysis, the results were compared with the 3-D fault zone distribution obtained from structural mapping of the Mina Ratones area on a scale of 1:1000, seismically derived structural data, drill cores and well log data. Furthermore, the range of the FI values that characterize the undeformed protolith and the damaged zone/fault core in Mina Ratones area are also determined.

3. Geological and structural setting

3.1. The Albalá Granitic Pluton

The Albalá Granitic Pluton is located in the southwest sector of the Iberian Massif (Central-Iberian Zone of Julivert et al. (1972)), which represents the westernmost segment of the European Variscan Belt (Pérez Estaún et al., 1991). The pluton is a concentrically zoned body, elongated in a N–S direction, with porphyritic biotite granites in the rim and fine-grained two-mica leucogranites in the core (Fig. 3). Major, trace and rare-elements suggest that the magmatic rocks form a continuous sequence ranging from granodiorites through monzogranites, granites to leucogranites (Gumiel and Campos, 1993; Enresa, 1996). Rb–Sr whole rock ages indicate intrusion ages of 302 ± 4 Ma (Enresa, 1996). The Albalá Granitic Pluton was emplaced in the epizonal rocks of the Schist–Grauwacke Complex

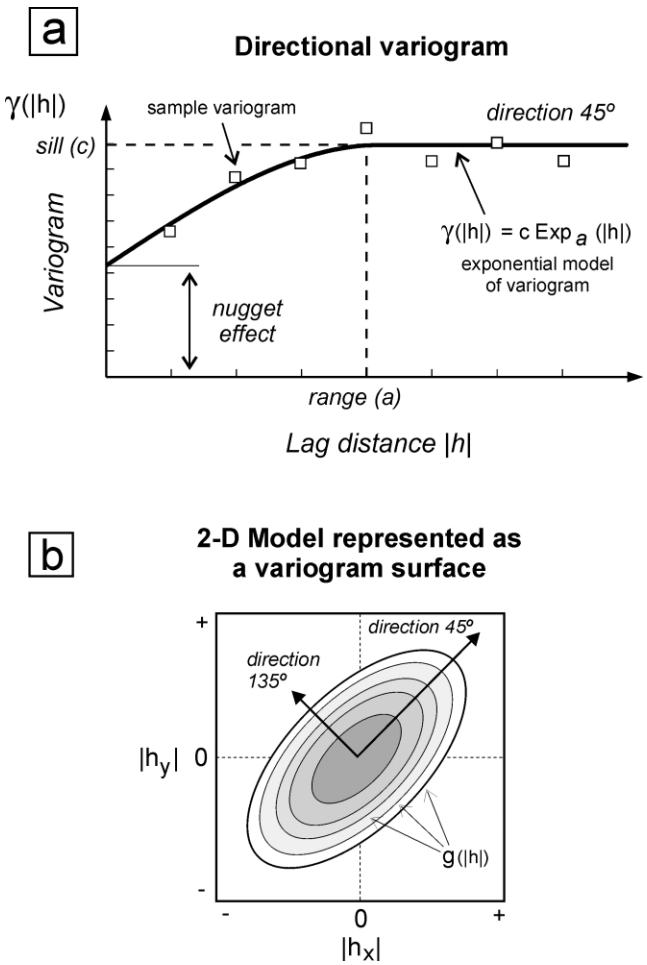

Fig. 2. Comparison between the sample variogram (squares) and the ideal exponential model used to generate FI fields by stochastical simulation. (a) Fitted 2-D exponential model viewed in a specific direction (45°), or directional variogram, and (b) its synthetic representation as a variogram surface. The exponential variogram model has a range (a) and a sill value (c).

(Upper Proterozoic to Lower Cambrian) and the fossiliferous formations of the Lower Ordovician (Gil and Pérez Rojas, 1982). In these materials, a Variscan S1 schistosity is recognized with a N–S to NNE–SSW trend and subvertical dip. S1 schistosity appears folded by a system of subvertical ductile shear zones with NW–SE trend and sinistral displacement, related to a second E–W directed shortening phase. The ensemble is also deformed by a set of ductile–brittle and brittle wrench structures, related to a third late-Variscan N–S to NNE–SSW directed subhorizontal shortening (Castro, 1986; Ortega et al., 1988; Díez Balda et al., 1990). The regional distribution of magmatic fabrics in the Albalá Granitic Pluton indicate that their emplacement was coeval with this third late-Variscan phase (Escuder Viruete, 1999).

Sn, W, As, P and U enrichment and mineralization events present in late-magmatic dykes are genetically related with the most differentiated leucogranitic hosted rocks (Reguilón, 1988; Reguilón et al., 1996). The uranium mineralization comes from the remobilization of this element, present in the host leucogranite, in the form of accessory uraninite. The mineralizing fluid-filled fractures are organized in a pattern which is consistent with late-Variscan strike-slip tectonics (Castro, 1986; Sanderson et al., 1991; Enresa, 1996). Mina Ratones is located in the central-southern sector of the Albalá Granitic Pluton (Fig. 4a). Two main NNE–SSW-oriented subvertical filons (27 and 27′ Dykes), with quartz, pitchblende, coffinite and black Fe–Mn oxides, were mined between 1955 and 1974. Approximately 125,000 tons of uranium oxides with a grade of 0.227% were extracted (Arribas, 1962; Martínez and Ramírez, 1966).

3.2. Post-Variscan deformation

The post-Variscan structural evolution of the Albalá Granitic Pluton has been established on the basis of fault kinematics and palaeostress analysis. This evolution includes three phases of brittle deformation related to different stress-field configurations, that cut and reactivate ductile and ductile–brittle late-Variscan structures (Enresa, 1996; Escuder Viruete and Pérez Estaún, 1998; Escuder Viruete, 1999). The first post-Variscan phase is extensional and produces the intrusion of Jurassic subvertical basic dykes (diabases), aligned on a NNE–SSW trend (Fig. 4b). The constant trend of these dykes at the regional scale indicates that σ_3 was subhorizontal and WNW–ESE to NW–SE directed.

The second post-Variscan (Tertiary) phase is characterized by the development of a system of conjugate strike-slip faults and associated mid- to low-angle thrusts. In the Mina Ratones area, strike-slip faults can be geometrically grouped into two distinct sets: the sinistral NNE–SSW to ENE–WSW and the conjugate dextral N–S to NW–SE (Fig. 4d). Tertiary thrust faults show an E–W to ENE–WSW trend and a N-directed sense of movement. The kinematics of all strike-slip and thrust faults suggest that σ_1 was subhorizontal and NNE-directed during this phase, characterized by a wrench stress configuration (Enresa, 1996; Escuder Viruete and Pérez Estaún, 1998). Many late-Variscan subvertical dykes and faults also have a NNE–SSW to NE–SW trend, and these structures are frequently reactivated during this phase as strike-slip faults (Fig. 4c).

At outcrop scale, the Tertiary strike-slip faults are defined by complex fault zones. These fault zones are characterized by abundant subparallel joints, shears and minor faults, with horizontal displacement <1 m. In the drill cores, the thickness of individual fault zones can vary between 0.1 and 18 m. Major fault zones are characterized by a <50-cm-thick core bordered by a fractured and faulted damage zone several meters thick, for example the hanging wall section of the North Fault (Fig. 5). Fault core is composed of reddish fine-grained cataclasite and gouge, which display a crude to well-defined foliation defined by lozenges and irregular zones of relatively less-deformed

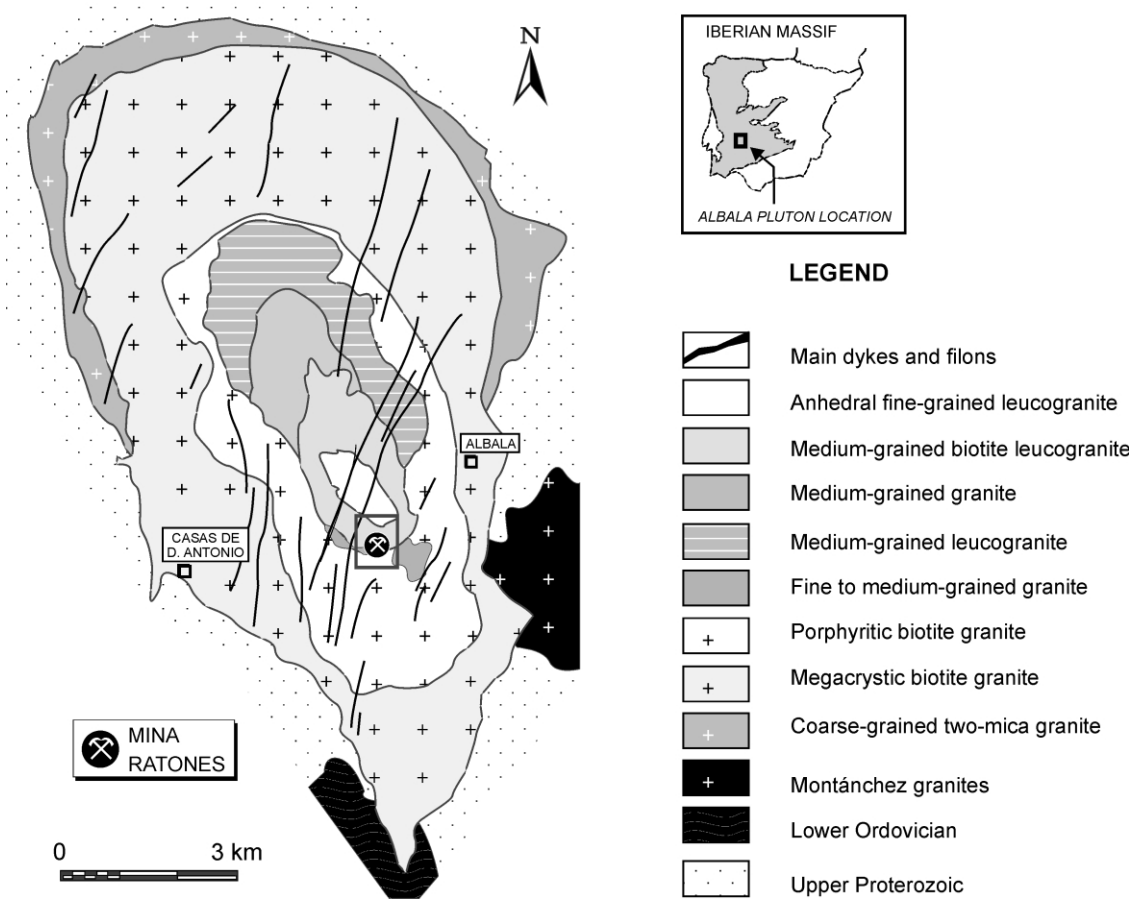

Fig. 3. Geological map of Albalá Granitic Pluton with location of the Mina Ratones area (Enresa, 1996; Escuder Viruete and Pérez Estaún, 1998).

protolith. The minor faults within the damage zone are narrow, 0.5–10 cm wide and are composed of variable foliated microbreccias and very fine-grained gouge. Contacts between cataclasite and undeformed granite are sharp along the narrow faults. Some of the fault core rocks contain secondary U-mineralization generated by remobilization of uranium in the fluid-phase through the fault zone network, during the reactivation of late-Variscan dykes as Tertiary strike-slip faults.

The third post-Variscan phase produced the partial reactivation of the previous structures and dykes as normal faults. The kinematics of fault system deduced from striated slickensides in the fault plane are compatible with an extensional stress field, with a subhorizontal and NNW- to N-directed σ_3, opposite to the previous Tertiary shortening, and even with a late radial extension (Fig. 4f; Enresa, 1996; Escuder Viruete and Pérez Estaún, 1998). Late normal fault cores are characterized by microbreccias, foliated cataclastic rocks and slightly colored gouges.

3.3. Fault zone architecture in the Mina Ratones area

Fault zone architecture in the Mina Ratones area has been established on the basis of field geology, structural analysis, seismic experiments, drill cores (SR-1 to 5) and sonic well-log data (Escuder Viruete and Pérez Estaún, 1998; Carbonell et al., 1999; Escuder Viruete, 1999; Jurado, 1999; Pérez Estaún, 1999; Martí et al., 2002). The 3-D fault distribution obtained for this area is shown in Fig. 6. The main structures identified are the North Fault, the South Fault and the 27 and 27′ Dykes. Other relevant brittle structures of minor size are the 474, 478, 285 and 220 Faults. Further, the seismic profiles suggest the existence of the 476 Fault (or dyke?) east of SR-3 well.

The 27 Dyke trends N028°E and dips E at 80–85° (Figs. 4a and 6). The Dyke has a thickness of 0.4–1.8 m and is composed of a cataclastic breccia of quartz, quartz-apatite, opaque chert and jasper fragments, cemented by sulphides, pitchblende, coffinite and black Fe–Mn oxides. The detailed structural and cartographic data of the structure suggest that the quartz-apatite fill is related to the late-Variscan ductile–brittle brittle wrench shearing. The adjacent granite is characterized by a pervasive hydrothermal green alteration (chlorite–epidote–sericite). The 27 Dyke was reactivated during the post-Variscan evolution as a Tertiary strike-slip dextral fault and a late normal fault. These movements produce a subparallel damage zone characterized by NNE–SSW to ENE–WSW-trending subvertical fractures, anastomosing slip surfaces, breccias, microbreccias, extensive white clay alteration and clay-rich gouge, as well as the

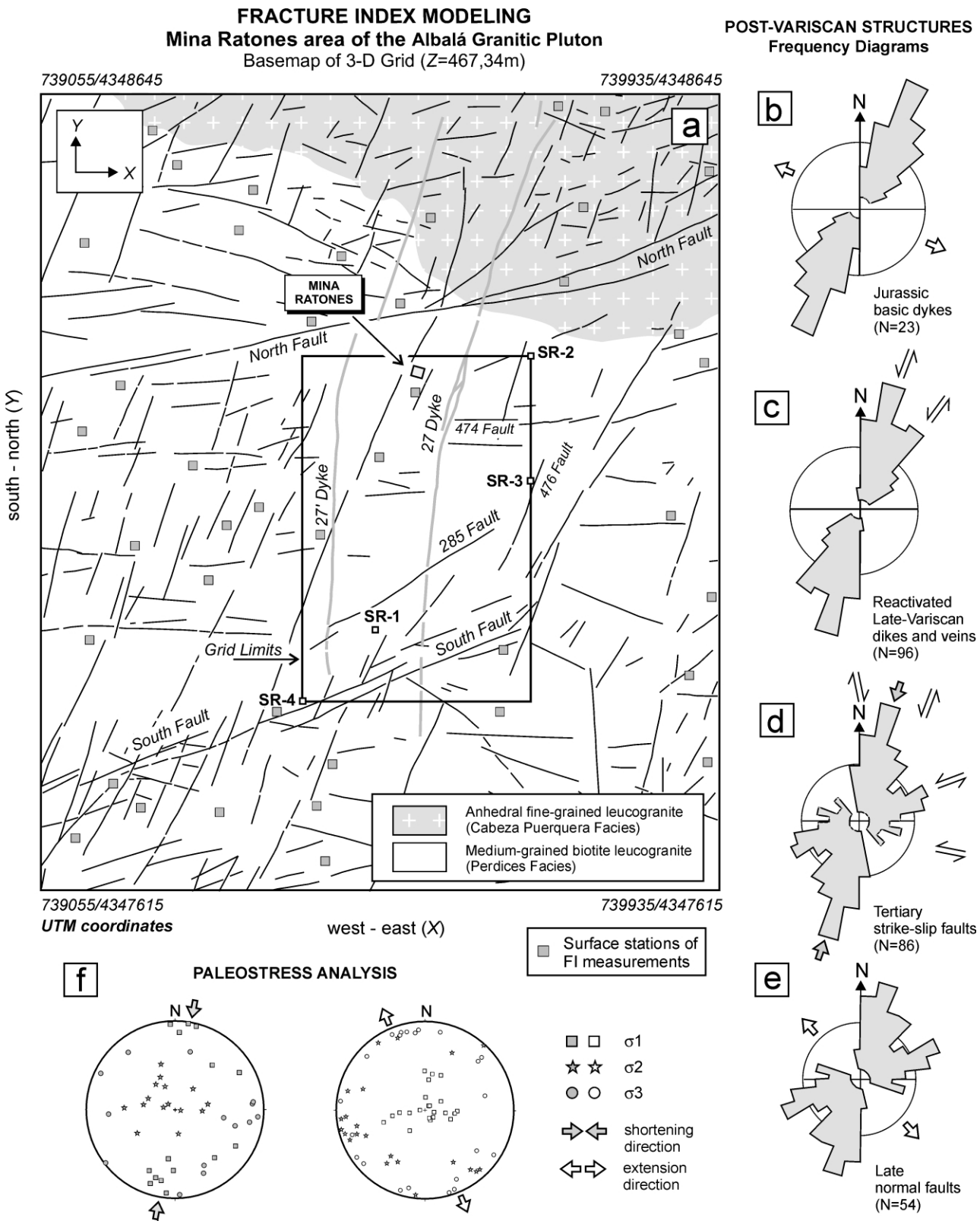

Fig. 4. (a) Structural map of brittle structures in the Mina Ratones area showing the location of the wells (SR-1 to 4) and surface outcrops where the FI was measured, and the top limits of 3-D grid used in the stochastic simulation; (b)–(e) rose diagrams of post-Variscan structures; (f) results of paleostress analysis carried out on Tertiary faults (Escuder Viruete, 1999).

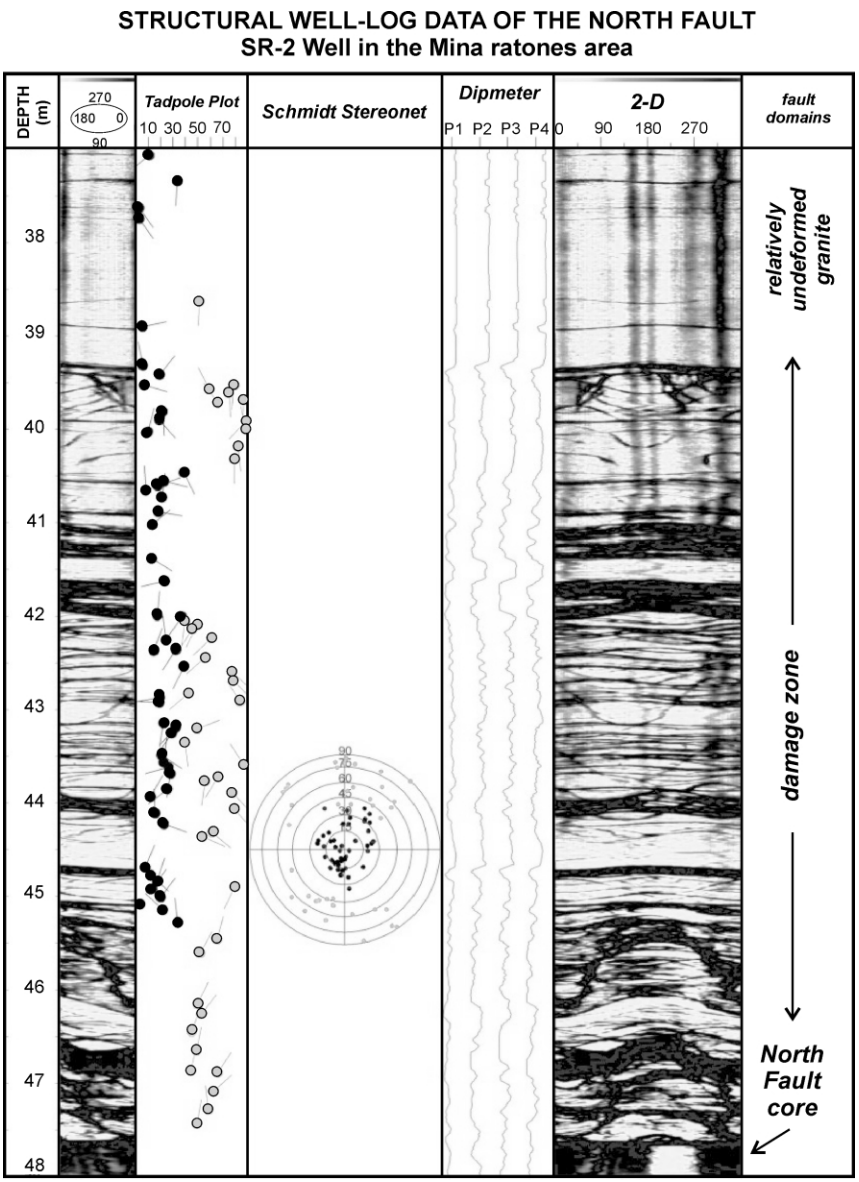

Fig. 5. Well-log data of the North Fault hanging-wall in the SR-2 borehole (Jurado, 1999). From left to the right, 3-D borehole televiewer (BHTV), fracture dip diagram, fracture poles stereonet, microresistivity dipmeter curves, 2-D image televiewer and, over the acoustical wave diagram, the black line defining the first arrival of P waves. Note the progressive increase of the fracture intensity (FI in this work) in the damage zone toward the North Fault core.

local remobilization of dissolved U that precipitated in open spaces as secondary autunite, torbernite and U-silico-phosphates. Numerous fault surfaces are grooved, striated and coated with finely comminuted red Fe–Mn oxides.

The 27 and 27′ Dykes are two related mineralized structures of subparallel trend (Figs. 4a and 6). The 27′ Dyke trends N014°E and dips W 75–80°, and becomes subvertical at 90 m depth. The Dyke core is defined by a quartz-rich breccia, mineralized with pitchblende and sulphur, hosted in an extensively fractured damage zone of hydrothermally altered granite. The post-Variscan reactivation of the structure shows dextral strike-slip faulting and a normal fault is also recognized.

Drill cores (SR-2 and SR-3 wells) and geophysical data suggest the North Fault has a N072°E to N080°E trend and a S dip of 55–65°, that decreases with depth to 30–40°. The related fault zone exposed at the surface has a width of 12–16 m and is characterized by high fracture intensity and an extensively altered granite (lehm). The approximately 15-m-thick section of North Fault zone recovered in the SR-2 well (Fig. 5) is defined by a fractured and faulted damage zone and a narrow fault core (70 cm). The damage zone is characterized by kinematically related mesoscopic fractures and small faults, grain-size reduction and brittle microstructures produced by cataclastic flow. Fracture frequency clearly increases toward the central fault core (Fig. 5). The fault core consists of an incohesive fine grained aggregate of kaolinite, smectite, and quartz, with some relic hydrothermal muscovite grains. A minor zone of brittle deformation and clay alteration recovered in the SR-3 well suggests that

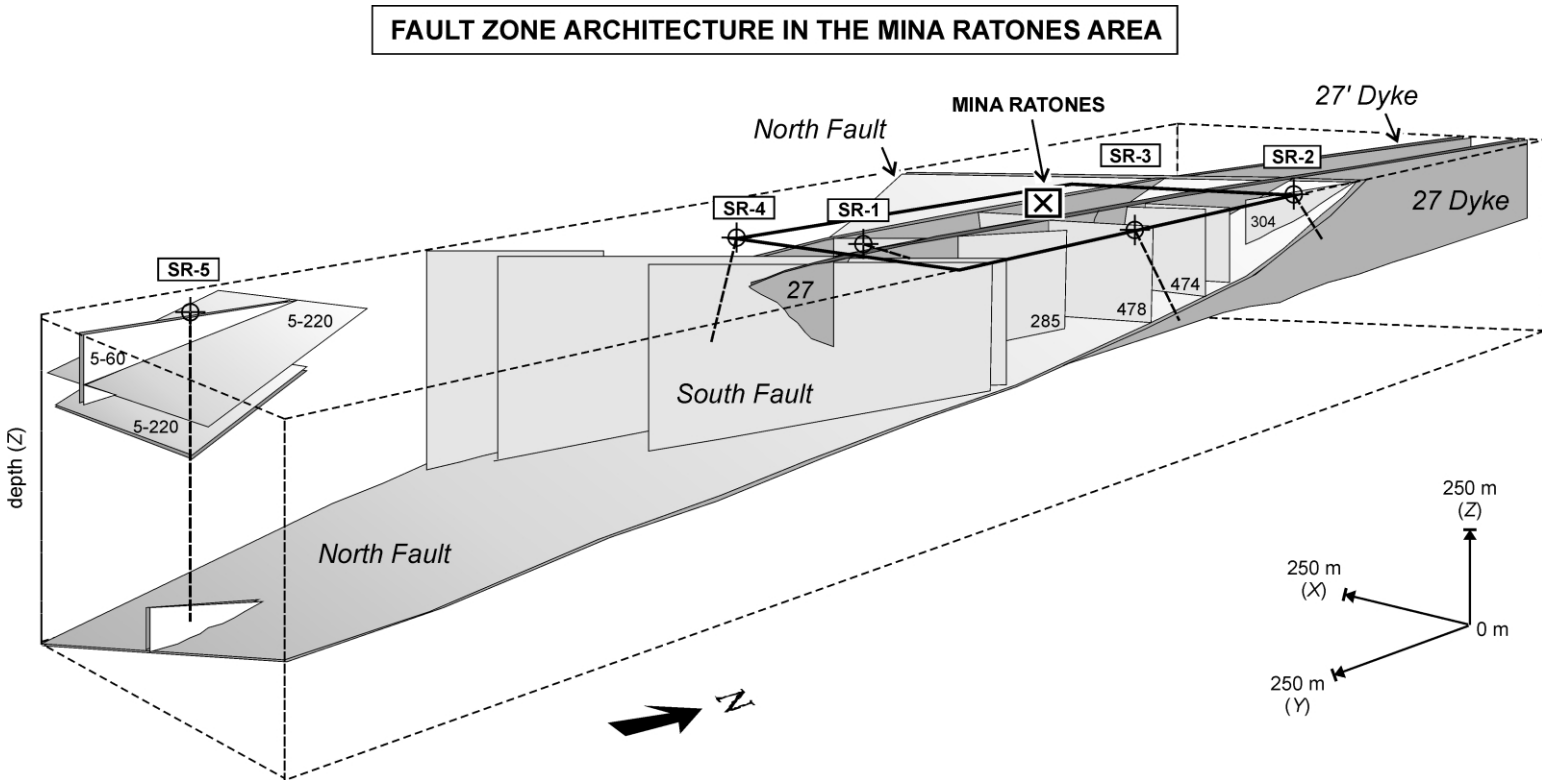

Fig. 6. Fault zone architecture of Mina Ratones area obtained from structural, seismic, core and well log data (Escuder Viruete and Pérez Estaún, 1998; Carbonell et al., 1999; Escuder Viruete, 1999; Pérez Estaún, 1999). The main identified structures are the North Fault, the South Fault and the 27 and 27′ Dykes. Other relevant brittle structures of minor size are 474, 478, 285 and 220 Faults.

the North Fault zone reduces in thickness with depth. Slickensides with a N–S trend on small subparallel faults in the damage zone indicates an inverse movement of the hanging-wall, and they suggest that the North Fault was firstly a N-directed Tertiary thrust. However, the structure was reactivated as a normal fault during the late extensional phase, when the hanging-wall block moved to the South (Escuder Viruete and Pérez Estaún, 1998).

The South Fault damage zone is defined by subvertical small faults and kinematically related fracture sets and joints, that form a 14–20-m-thick brittle shear-zone of strike-slip sinistral movement. Small faults have a N064°E to N078°E trend and a N dip of 68–82°. The existence of subhorizontal slickensides along these faults suggest their reactivation during the Tertiary phase of wrench tectonics. However, late N-directed, normal slip is observed along some planes of these small faults. The South Fault core rocks recovered in the SR-4 well are microbreccias and white clay-rich gouges.

The 474 and 474′ Faults are two high-dip subparallel structures that trend N064°E to N076°E. The fault damage zones are 5–8 m thick and are characterized by a high density of small sinistral-slip faults and joints. Both structures connect toward the W with the 27 Dyke. The 285 brittle structure is also a sinistral strike-slip fault with a N052°E to N060°E trend and subvertical dip. The 220 Fault has been identified in the SR-5 well and consists of a late normal fault with an E–W trend, 25–45° dip and southern hanging-wall block.

4. Geostatistical analysis

4.1. Geostatistical methodology and data collection

The methodology applied to model the spatial distribution of fault zones in this study has several steps, which are typical of other geostatistical analyses (Deutsch and Journel, 1992; Pannatier, 1996; Goovarets, 1997; Pebesma and Wesseling, 1998; Kupfersberger and Deutsch, 1999).

The first step consisted of building a georeferenced database of FI, a measure of the fracture intensity per unit length in a discrete domain of the granitic massif. FI was measured on selected surface outcrops (limited in number and spatial distribution) and in cores of four near vertical boreholes drilled at Mina Ratones (Fig. 4a). However, traditional fracture spacing measures have inherent geometric biases, which can lead to inaccurate representations of the true fracture pattern. These linear sampling biases were eliminated utilizing a trigonometrical correction following Terzaghi's (1965) approach and the techniques included in La Pointe and Hudson (1985). Consequently, structural discontinuities were measured in all outcrops along two scanlines 15–25 m length, that cross one another at nearly perpendicular angles. Along scanlines, the point of intersection of the fractures with the scanline is recorded and, in the case of faults, throw, dip-direction, dip-angle and vector of movement were also recorded for further geometric and kinematic analysis. From fracture spacing data unbiased rosettes and stereograms of fracture frequency (La Pointe and Hudson, 1985) were compiled, which more closely approximate the true geometry of the fault zone system and allow computation of the overall fracture intensity in each outcrop.

In the oriented cores drilled at Mina Ratones, FI was obtained by subtracting consecutive intersection distances of fractures with the well-axis. The linear sampling bias in fracture frequency measurements was also eliminated using the trigonometrical correction of Terzaghi (1965). The acoustic records obtained from ultrasound (borehole televiewer, BHTV) provided an oriented image of the well wall (Fig. 5; Jurado, 1999), where dip-direction and dip-angle of small faults and joints were determined, and also permit discrimination of the tectonic fractures from the induced fractures as a consequence of core perforation and extraction. The well log data of FI and $X–Y–Z$ coordinates of each measurement are stored in ASCII files of similar format to *Geo-Eas* and *GSLIB* data-files (Englund and Sparks, 1991; Deutsch and Journel, 1992). Well log data of FI contain column-wise data for a series of well-depths with 1 m of spacing.

The second step is to obtain the sample directional variograms, where it is possible to detect directional anisotropies in the pattern of spatial continuity (Isaaks and Srivastava, 1989; Pannatier, 1996). Directional variograms were calculated in NW–SE, N–S, NE–SW and E–W directions, as well as the vertical direction. The obtained areal variogram shows how spatial continuity of FI data varies in the different subhorizontal directions. In the case of Mina Ratones, the main spatial continuity directions of FI should coincide with the main trends of small scale fractures and mapped faults, Variscan and post-Variscan in age. Sample vertical variograms usually reach high variance values in much shorter distance (Kupfersberger and Deutsch, 1999).

The third step is fitting a theoretical 3-D variogram model with the directional experimental variograms through an iterative process (Isaaks and Srivastava, 1989; Deutsch and Journel, 1992; Goovarets, 1997; Kupfersberger and Deutsch, 1999). The geometry of this 3-D variogram defines the parameters of the geostatistical model (Fig. 2). 3-D model parameters permit the calculation of an areal correlation length ratio (Cr_A = major/minor correlation lengths) and the vertical correlation length ratio (Cr_V = major/vertical correlation lengths), as well as the directional anisotropy of the FI, or the direction of greatest horizontal continuity (in degrees clockwise from the north). The model parameters of the 3-D variogram model are introduced as a stochastic representation procedure, or geostatistical conditional simulation (Gómez Hernández and Srivastava, 1989; Deutsch and Journel, 1992), between the measured data of FI. As a result, the total set of FI values, measured in

the wells and simulated, form a mesh of points or grid that describes the continuous value of the fracture intensity in 3-D. In this study, a 3-D grid is a series of equal-size blocks (or cells) with a value of FI assigned to each block. The 3-D grids can be edited as views of the FI block models, surface grids for a specified layer, cross-sections, grid slices and 2-D maps of various types (pixel and contour maps). Multiply simulated realizations allows an assessment of uncertainty with alternative realizations possible (Deutsch and Journel, 1992; Gómez Hernández and Cassiraga, 1994). The calibration of the grids was achieved by comparing them with the structural cartographic data, geophysical seismic profiles and 3-D models for fault zone architecture in Mina Ratones (Escuder Viruete and Pérez-Estaún, 1998; Carbonell et al., 1999; Escuder Viruete, 1999; Pérez Estaún, 1999; Martí et al., 2002).

4.2. Descriptive statistics of FI

Fig. 4a shows the location of wells where the FI was measured near Mina Ratones and the top of the simulated 3-D grid. The grid consists of a rectangular area whose NE and SW vertices coincide with the position of the SR-4 and S-2 wells, respectively. The wells were lithologically and structurally correlated along the vertical section of Fig. 7, whose length is 538.8 m. Table 1 includes a summary of descriptive statistics of the FI sample. For a total of 428 estimates, measured minimum and maximum values of FI in the wells are 0.01 and 26.0 m^{-1}, respectively. The resulting mean value for FI is 6.224 m^{-1}, with a standard deviation of 4.330 and a sample variance of 18.751. The frequency distribution is clearly uni-modal (Fig. 8), with a positive asymmetry and 4.0 as the mode value. The FI values approximate a negative exponential distribution rather than a log-normal, as the 0.0–2.0 class interval is near the highest (rather than zero) frequency. The frequency distribution has skewness of 1.34 and kurtosis of 2.75.

Table 1
Descriptive statistics of fracture index (FI in m^{-1} units) data for the Mina Ratones area

Borehole	SR-1	SR-2	SR-3	SR-4	All
Count	167	66	73	122	428
Minimum	0.01	0.01	0.01	0.01	0.01
Maximum	24	26	18	13	26
Mean	5.13	8.09	5.53	7.11	6.22
Standard deviation	3.91	6.56	3.69	3.04	0.21
Skewness	1.52	0.96	1.04	0.16	1.34
Sum					2664.1
Median					5.0
Mode					4.0
Standard deviation					4.33
Sample variance					18.75
Kurtosis					2.748
Range					25.99

4.3. FI directional, vertical and areal variograms

Four exploratory directional variograms of the FI were obtained along the NE–SW, N–S, NW–SE and E–W directions, as well as the vertical variogram (Fig. 9). These directional variograms were computed with *GSLIB* (Deutsch and Journel, 1992), *Variowin* (Pannatier, 1996) and *GSTAT* (Pebesma and Wesseling, 1998) geostatistical software. *Variowin* software allows identification of (z_i, z_{i+h}) pairs that have a strong influence in the spatial continuity. In the horizontal variograms, the lag distance h and the number of lags are 85 m and 8, respectively, covering a distance of 680 m for a tolerance angle of 30°. In Fig. 9a and b, the variable correlation length obtained as a function of variogram direction is observed, varying the range of the sample variograms between 19.8 (vertical direction), 80 (NW–SE direction) and 508 m (NE–SW direction). As a consequence, FI is anisotropic; its pattern of spatial continuity changes with direction. Also, the resulting anisotropy of the FI is geometric (Kupfersberger and Deutsch, 1999); the horizontal and vertical variograms reach the same sill, but the range in the vertical direction is 1/20 of the maximum range in the NE–SW horizontal direction. The areal variogram of Fig. 9c was plotted by taking 10 lags of 100 m along the *X*-direction (east) and the *Y*-direction (north), and visualized in the form of a variogram surface. The areal variogram shows that the FI has maximum spatial continuity along the NE–SW and N–S directions and minimum spatial continuity following the NW–SE and E–W directions. As was expected for the Mina Ratones area, the maximum continuity obtained along NE–SW direction represents the mean trend between the NNE–SSW and ENE–WSW fault sets, which define a romboidal pattern in the structural map of Fig. 4a. The main NNE–SSW fracture set appears also defined by relatively high values of spatial continuity along the N–S direction of areal variogram.

4.4. 3-D FI modeling

The sample directional variograms can be used to fit a theoretical 3-D variogram model that describes the spatial continuity of FI. Being the crucial part of most geostatistical studies, variogram modeling should be done interactively (Deutsch and Journel, 1992). For this analysis *Model* (Pannatier, 1996), and *GSTAT* (Pebesma and Wesseling, 1998) software were used. Both programs provide an interactive user interface for graphical display and fit the selected variogram model function to the points of the sample variograms simultaneously along several directions.

In Fig. 9b, the fitted horizontal variograms appear as convex curves defined by the following expression:

$$\gamma(h) = 15.959 \times \mathrm{Exp}_a(h) \quad (2)$$

where $\mathrm{Exp}_a(h) = \{1 - e^{(-3h/a)}\}$ and a is the practical range, that is, the distance at which the variogram value is 95% of

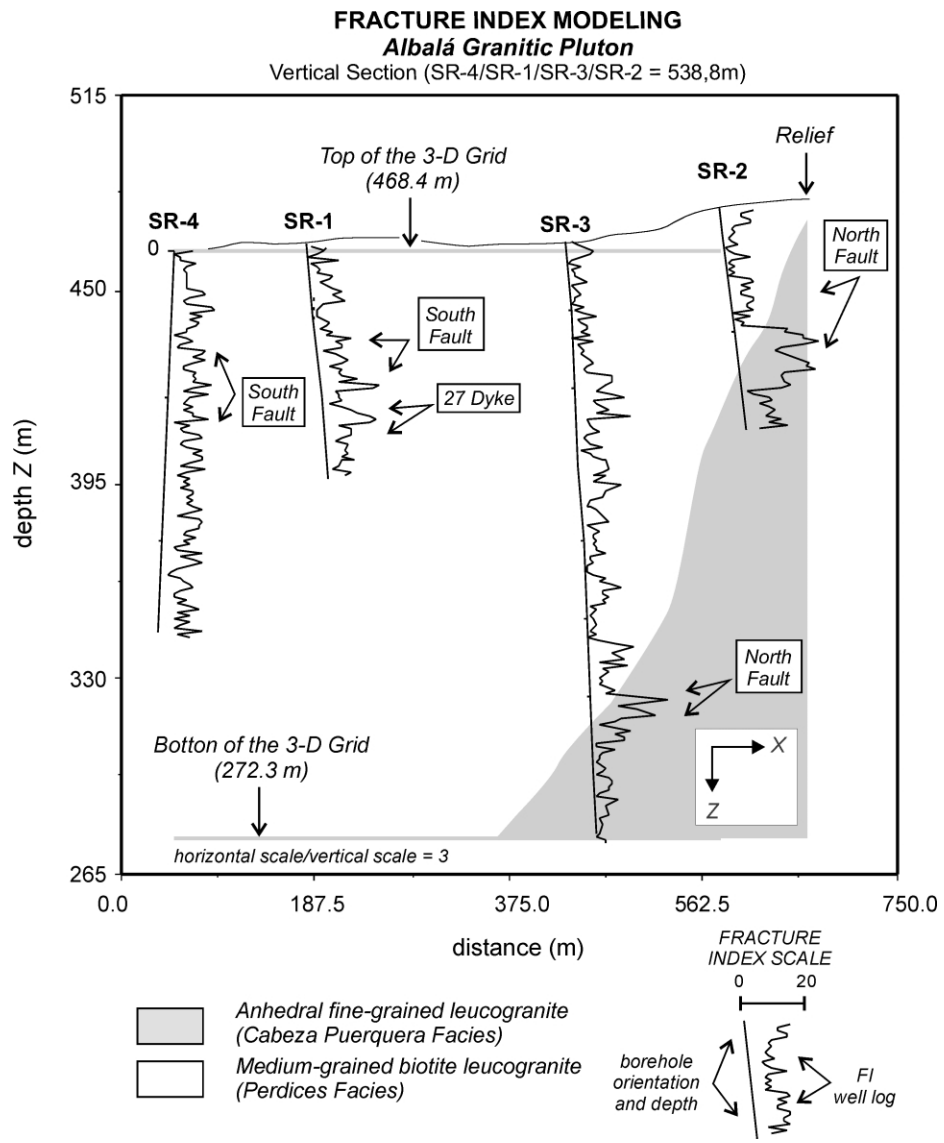

Fig. 7. Vertical section showing SR-4/SR-1/SR-3/SR-2 well-log data of FI and the dimensions of the 3-D grid.

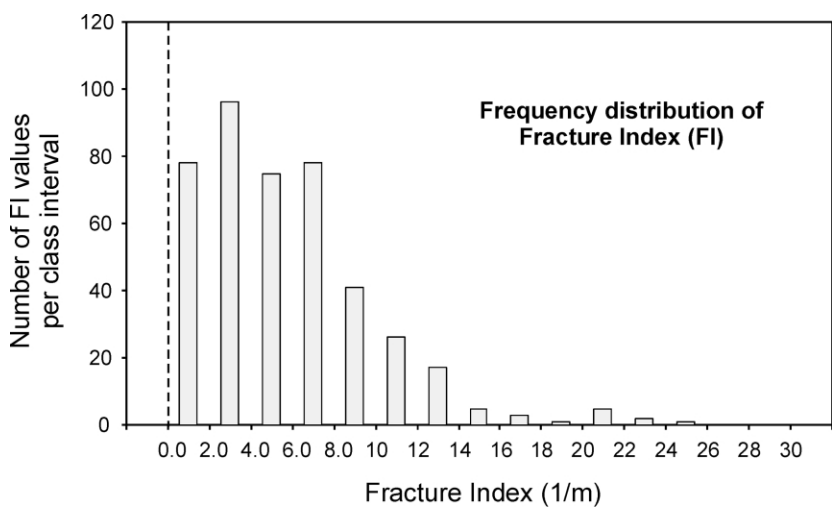

Fig. 8. Frequency distribution (histogram) of FI. For an explanation see the text and Table 1.

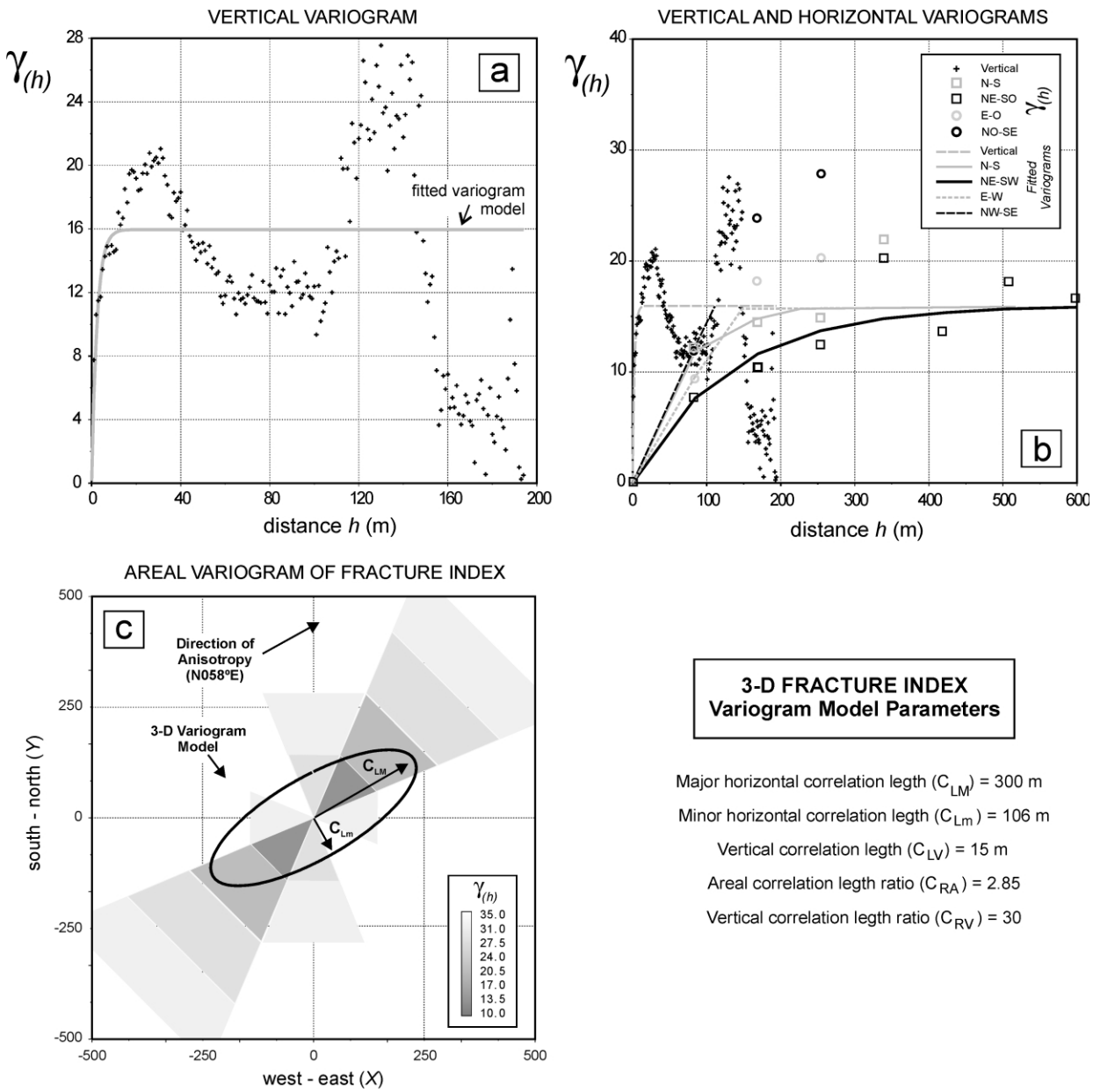

Fig. 9. FI variography: (a) sample vertical variogram; (b) sample vertical and horizontal variograms; and (c) modeled areal variogram. The points are the $\gamma|h|$ values calculated at each lag of 1 m (vertical variogram) and 85 m (horizontal variograms). The convex curves are the fitted exponential model variogram.

the sill. This model reaches its sill asymptotically and has linear behavior at the origin (Pannatier, 1996). The resulting nested model of spatial continuity of FI is exponential and their parameters are defined by nugget = 0.0, range = 547.7 and sill (variance) = 15.96, with a direction of anisotropy of 058° in the horizontal plane. The measure of a good fit between sample variograms and the model variogram is indicated by the curve fit error of 9.54. The vertical model variogram is defined by a similar expression but with a range of 19.8 m (Fig. 9a). In summary, the obtained 3-D nested model of spatial continuity of FI is the sum of an isotropic nugget effect and a simple anisotropic structure of exponential type. The selected ellipsoid of correlation for 3-D gridding results in major, minor and vertical correlation lengths of 300, 106 and 15 m, respectively (Fig. 9c). The areal and vertical correlation length ratios of the ellipsoid are 2.85 (Cr_A) and 30.0 (Cr_V).

4.5. 3-D FI simulation

With the parameters of the spatial continuity model previously defined, conditional simulation was used for modeling FI in 3-D (Gómez Hernández and Srivastava, 1989; Deutsch and Journel, 1992; Gómez Hernández and Cassiraga, 1994; Cassiraga and Gómez Hernández, 1996). The volume of rock massif covered by the simulation is framed between two coordinate vertices 739412/4347882/273.3 (*X*/*Y*/*Z* minimum, bottom of SR-4 well) and 739690/

4348293/467.3 (*X*/*Y*/*Z* maximum, top of SR-2 well). This volume (Fig. 4a) is discretized in individual cells of dimensions 3.0, 3.0 and 2.2 m, throughout the east (*X*), north (*Y*) and vertical (*Z*) directions, respectively. These dimensions are similar in size to the scanlines used for the determination of FI in the well-cores. The corresponding number of cells throughout *X*, *Y* and *Z* directions is 94, 138 and 90, resulting in a total of 1,167,480 cells. For 3-D stochastical modeling of FI, the *sgsim* (sequential Gaussian simulation) routine of *GSLIB* library (Deutsch and Journel, 1992) were used. The total number of alternative grids of FI computed by multiple geostatistical simulation was 10, selecting a final 3-D grid of FI as an average grid of all simulated realizations. Results are shown in Figs. 10–14.

4.5.1. Surface FI simulation

Fig. 10 shows a top view of the 3-D grid of FI ($Z = 467.3$ m) obtained as a result of the simulation. The grid, expressed as grayscale pixel-map, shows zones with high and low values of FI. More gray tone zones ($FI > 2.5\ m^{-1}$) are elongated following the NE–SW to ENE–WSW direction, which coincides with one of the more frequent fracture directions at all scales in the Mina Ratones area (Escuder Viruete and Pérez-Estaún, 1998; Escuder Viruete, 1999). In the central and SE sectors of the gridded area, the estimated FI is $<2.5\ m^{-1}$ and individual ENE-striking bands are characterized by low fracture intensity. To the W and NW of the top grid (Fig. 10), an elongate transitional zone appears toward a more fractured domain, defined by estimated $FI > 4.2\ m^{-1}$. A general observation in surface outcrops of Mina Ratones is that, in the damage zone of the main faults, the measured value of the FI increases in a normal direction toward the fault core. This fault density gradient adjacent to major strike-slip faults (and related brittle strain) has been also previously recognized by Caine et al. (1996), Little (1996) and Schulz and Evans (2000). In this sense, it is interesting to compare the distribution of FI values predicted by geostatistical simulation in the surface (2-D) with the superposed traces of the main mapped faults and dykes.

As observed in Fig. 10, darker bands of greater FI and the zones with a high fault density, or with faults of greater length, are well correlated. This is especially valid in the 27 and 27′ Dykes, and along a ENE–WSW directed band, located in the SE sector of the Mina Ratones, which coincides with the traces of the 285 and South Faults. Also, framed by subvertical faults of great length and characterized by a low cartographic fracture density, a sector with

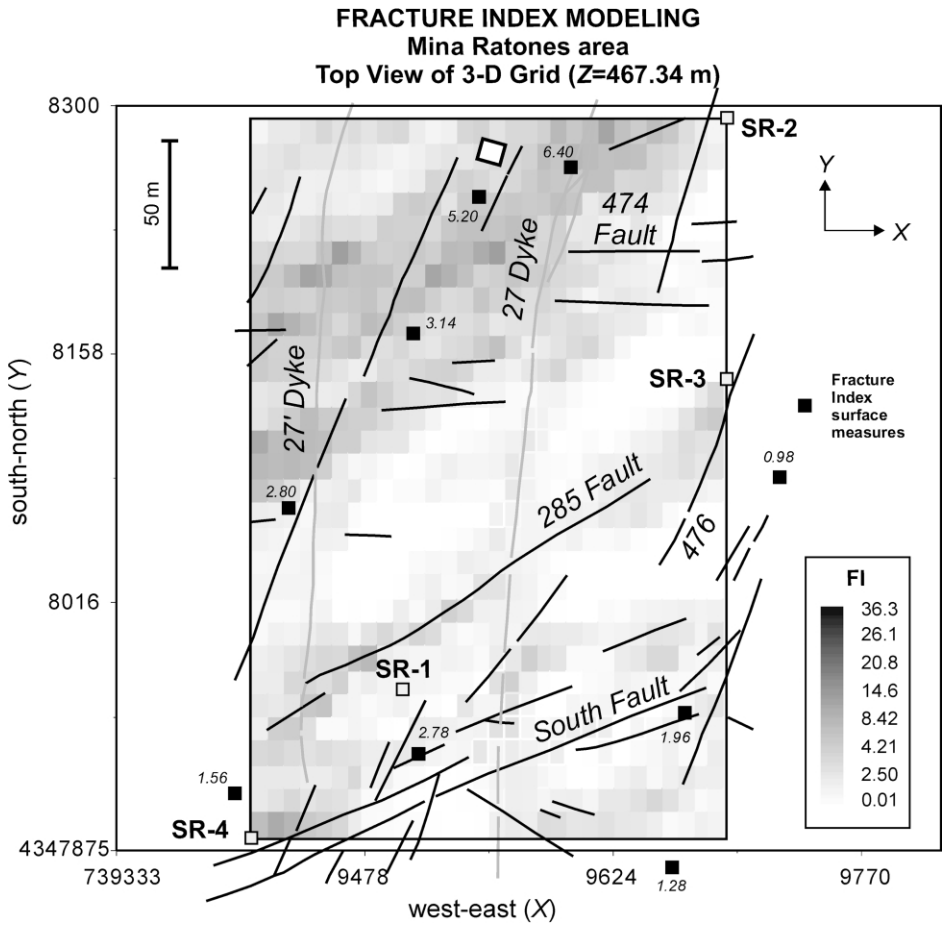

Fig. 10. Top view of the 3-D grid of FI ($Z = 467.3$ m) resulting from geostatistical simulation and the traces of the main mapped faults and dykes in the Mina Ratones area.

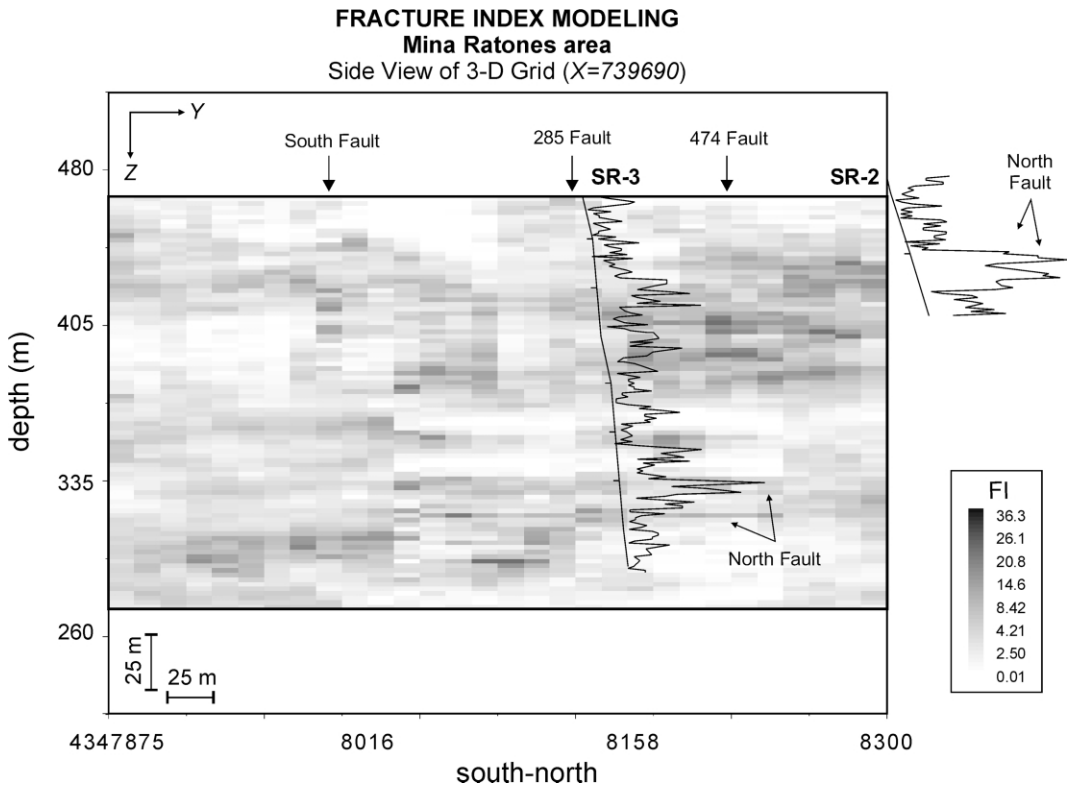

Fig. 11. Side view of the 3-D grid of FI ($X = 739690$) resulting from geostatistical simulation and the logs of FI in the SR-2 and SR-3 wells.

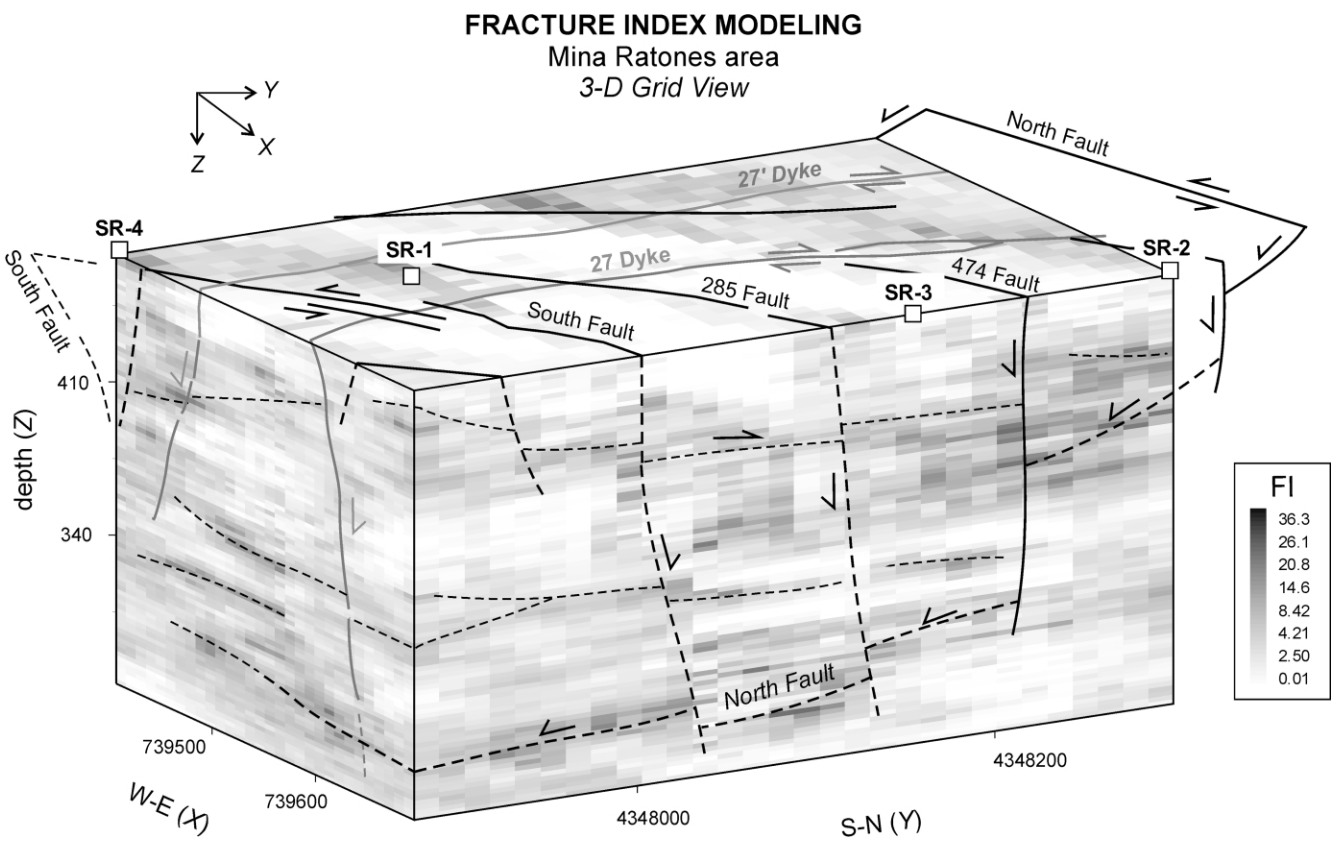

Fig. 12. Relationships between fault zone architecture and the 3-D grid (pixel-map) of the FI in the Mina Ratones area, looking from the SE (see text for an explanation).

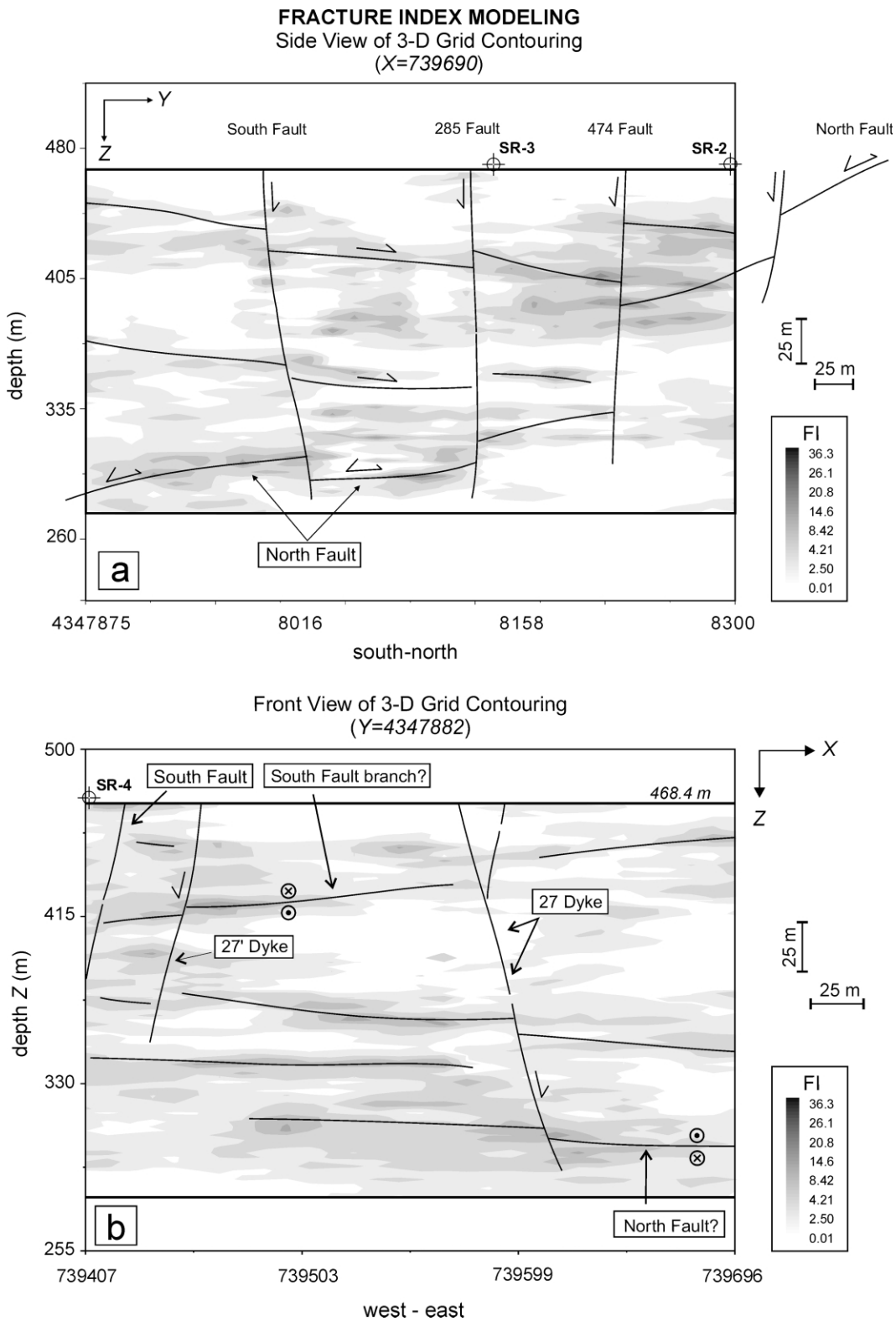

Fig. 13. (a) Side and (b) frontal views (contoured maps) of the 3-D grid of FI resulting from geostatistical simulation. (c) N–S high resolution seismic reflection profile (Carbonell et al., 1999; Martí et al., 2002) showing the location of SR-2 and SR-3 boreholes, and where reflections image structures as North, 474 and 285 Faults. See text for an explanation.

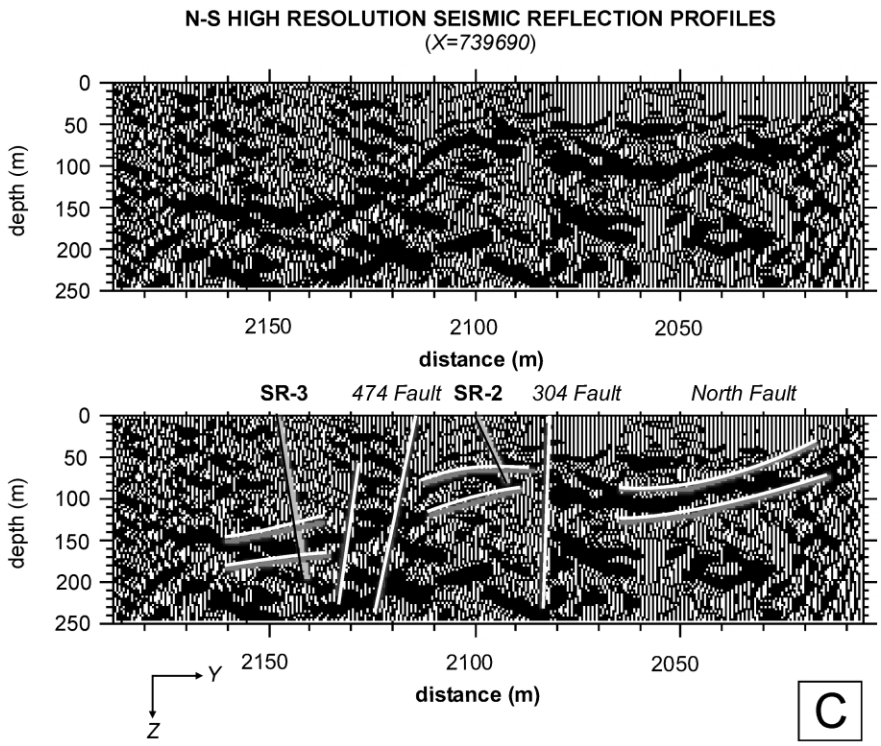

Fig. 13 (*continued*)

white tones of low FI is defined in the central portion of the grid. Therefore, the obtained distribution of the FI and its correlation with mapped faults permits us to distinguish two structural domains: elongate bands of fracture zones, and rhomboidal blocks located between them. As has been suggested by Escuder Viruete et al. (2001), the construction of grids of FI permits the quantitative structural characterization of the granitic massif in 2-D. Both structural domains probably correspond with the protolith and the damage zone/fault core in the model for fault zone architecture of Caine et al. (1996). Though a threshold value of the FI that separates both structural domains is not clearly observed, FI $> 4.2\ m^{-1}$ in the fracture zones and FI $< 2.5\ m^{-1}$ in the individualized blocks.

4.5.2. -D grid of FI

Fig. 11 shows a side view of the same 3-D grid of FI, following a N–S directed vertical section that includes the SR-2 and SR-3 wells ($X = 739690$). On the side view, the logs of the FI measured in cores of these wells have been superposed. As observed in the figure, wide zones of gray tones exist in the section indicative of a simulated relatively high FI ($>4.2\ m^{-1}$). These zones define elongated bands that are probably correlated with the position of main fractures, in particular, the North Fault (see below). The bands also delimit white tone regions of low FI ($<2.5\ m^{-1}$) related with blocks of less deformed granite.

Fig. 12 includes the 3-D grid of simulated FI, looking from the SE, as well as the surface location of the wells. In 3-D, the cells with relatively high values of the FI define irregular surfaces that could be inferred to be related to faults. These surfaces have moderate to low dip angles to the S and the N. Also, groups of stacked cells with a high FI are observed in the grid, possibly related to subvertical structures, as the South Fault. High FI surfaces intersect the top of the 3-D grid along NNE- and ENE-directed traces and coincide with the trends of the main mapped structures. For example, the 27 Dyke remains visualized in the frontal view of the 3-D grid ($Y = 4347882$) as a NNE–SSW-trending structure with an eastern high dip, and the 285 and 474 Faults are defined in the side view ($X = 739690$) as subvertical ENE–WSW-trending structures.

The structural interpretation of the 3-D model distributions of FI is visualized better in Fig. 13a and b. These figures show the superposition of 3-D contouring of FI and the trace of the main faults and dykes of the Mina Ratones area. The individual values of FI in each cell are contoured. As observed in Fig. 13a, the zones with a high FI define surfaces inclined at moderate to low angles in N and S directions. In general, these zones are well correlated with core sections of very fractured granite or reflections in the seismic profiles (Fig. 13c). These fracture zones and reflections were identified as the North, South, 474 and 285 Faults. The structural interpretation of well core data and seismic profiles allows us to deduce small jumps in reflections corresponding to the North Fault and other structures (Carbonell et al., 1999; Pérez Estaún, 1999; Martí et al., 2002). These jumps are of metric–decametric scale

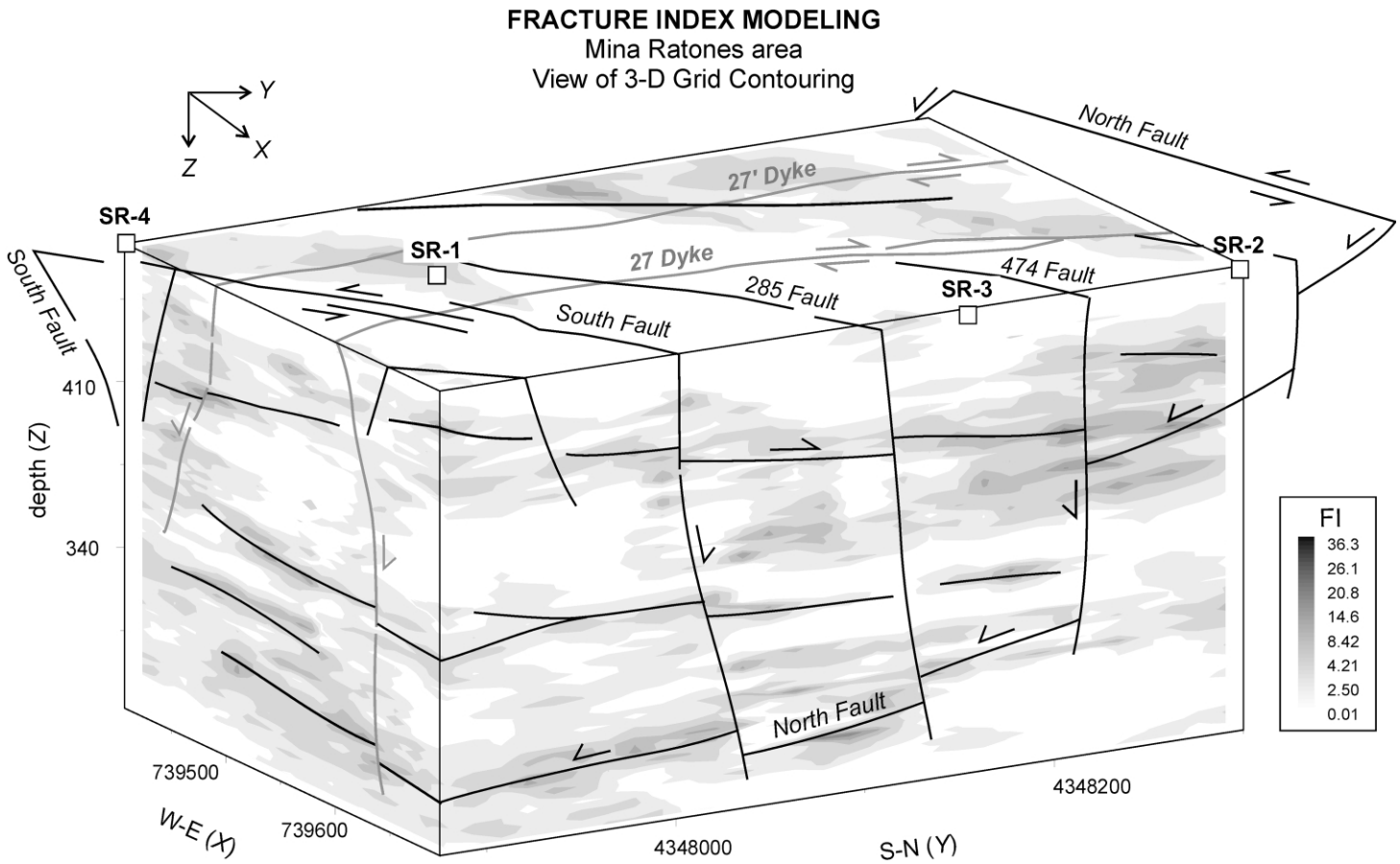

Fig. 14. Relationships between fault zone architecture and the 3-D grid (contouring) of the FI in the Mina Ratones area, looking from the SE. Two structural domains in base to the FI values are defined: variably irregular fault zones (FI $> 4.2\ m^{-1}$, gray tones) and rhomboidal blocks of relatively undeformed granite located between them (FI $< 2.5\ m^{-1}$, white tones).

and are imaged also by the 3-D distribution of the FI obtained from geostatistical simulation (Fig. 13a). The jumps are a consequence of the normal reactivation of the subvertical Variscan and post-Variscan structures during the latest extensional deformation. As observed in the side and frontal views of Fig. 13, the North Fault surface is offset by the South, 285 and 474 Faults, as well as the 27 Dyke.

Fig. 14 shows the results of contouring FI estimated values in the 3-D grid, and at the model looking from the SE. The view constitutes an image of the 3-D distribution of FI in the Mina Ratones area. This image is consistent with architecture of the main fault zones, which basically consists of two families of subvertical structures with NNE–SSW to N–S and ENE–WSW trends, which displace the surfaces of the North Fault and other related low angle faults. The late normal reactivation of 27 and 27′ Dykes also displace the North Fault surface. As is shown in Fig. 14, the high FI bands adjacent to major faults intersect in the 3-D grid defining rhomboidal blocks of relatively less fractured granite. Therefore, the construction of 3-D grids of the FI in granitic areas affected by brittle tectonics permits the quantitative structural characterization of the rock massif. The existing correlation between fault zones of great length and domains with high values of FI, allows for a model characterization of the rock massif in zones with few outcrops or limited borehole data, where the existence of important faults or fracture networks have not been previously detected. However, because the wells in the Mina Ratones area oriented along a NE–SW straight line, FI simulations in the NW sector of the 3-D grid are less rigorous. On the other hand, and due to the different aerial and vertical correlation length ratios (of an order of magnitude), the geostatistical simulation better defines the faults with moderate and low dips.

Finally, a 3-D grid of the standard deviation of the multiple geostatistical simulation was calculated from the 10 different values of FI estimated in each cell. The obtained standard deviation is lower in the low FI rhomboidal blocks ($\sigma < 0.22$) and, generally, higher in the high FI bands ($0.90 < \sigma < 1.52$) spatially associated with the main fault zones in the Mina Ratones area. These relationships are equivalent to those obtained by Escuder Viruete et al. (2001) and indicate that the uncertainties in the estimation of the FI would be greater for the fault zones than in the blocks located between them.

5. Conclusions

The main objective of this work is to quantitatively characterize the fault system of the Mina Ratones area in three dimensions from the spatial distribution of FI (fracture intensity in discrete domains of the rock massif) obtained from cell-based stochastic modeling and simulation. To calibrate the results of geostatistical modeling, seismic profiles, well core structural analysis and a detailed structural map of the Mina Ratones area on a scale of 1:1000 were completed. The resulting 3-D grids describe the continuous values of FI for the Mina Ratones area and constitute an image of fault architecture in the granitic massif.

3-D grids, expressed as block (cell) models or contouring (isosurfaces of FI), show high and low FI zones. The correlation of these zones with mapped faults allows identification of two structural domains in the Mina Ratones area: variably irregular surfaces of high FI and rhomboidal blocks of low FI located between them. High FI domains are interpreted as fault zones, since there is a good correlation at the surface between these domains and the traces of the main mapped fault zones. Low FI blocks correspond to less fractured granite. The contact between both domains is gradual in both field observations and model results. Constrained by seismic profiles and well core structural data, this correlation permits the modeling of continuity at depth of the major structures, such as the North and South Faults, or 27 and 27′ Dykes. The structural domains are interpreted to correspond with the damage zone/fault core and the protolith in the model for fault zone architecture of Caine et al. (1996). Though a threshold value of FI that separates the structural domains is not clearly defined, the fault zones generally result in FI values $>4.2\ m^{-1}$ and the blocks with FI values $<2.5\ m^{-1}$. Therefore, the construction of grids of the FI in granitic areas affected by strike-slip brittle tectonics, such as Mina Ratones, permits the quantitative structural characterization of the rock massif.

Further, this characterization permits volumetric calculations of FI in the granitic rock massif that have predictive value. For example, considering a threshold value for the FI of $4.5\ m^{-1}$ that separates relatively undeformed protolith and damage zone, the volume of rock with $0.01 < FI < 4.5\ m^{-1}$ is $8{,}374{,}618\ m^3$ at Mina Ratones. The existing correlation between FI and major fault zones can be applied to the characterization of the rock massif, even in zones with minor outcrops or distant to the boreholes and where the main fault zones may not have been detected. Finally, further development of geostatistical methods described in this study will include the 3-D modeling and simulation of porosity and permeability in fractured granitic massifs, taking into account pumping tests and geophysical well log data as well as P- and S-wave velocities.

Acknowledgements

This work represents part of the structural results of a multi-disciplinary project carried out for the environmental restoration of old uranium mines supported by ENRESA. Discussions with many colleagues of the CIEMAT, Universidad Politécnica de Cataluña and AITEMIN have contributed greatly to our understanding of faults at Mina Ratones. We thank J.S. Caine, T.T. Cladouhos and

T. Blenkinsop for their critical constructive and helpful reviews.

References

Arribas, A., 1962. Mineralogía y Metalogía de los yacimientos españoles del uranio: Los Ratones, Albalá (Cáceres). Estudios Geológicos. Vol. XVIII, Madrid.

Barton, C.C., Larsen, E., Page, W.R., Howars, T.M., 1988. Characterising fractured rock for fluid flow, geomechanical and paleostress modeling: methods and preliminary results from Yucca Mountain, Nevada (methods for parameterizing fracture characteristics at the scale of large outcrops). U.S. Geological Survey, Bulletin, March 3.

Caine, J.S., Forster, C.B., Evans, J.P., 1993. A classification scheme for permeability structures in fault zones. Eos (Transactions, American Geophysical Union) 74, 677.

Caine, J.S., Evans, J.P., Forster, C.B., 1996. Fault zone architecture and permeability structure. Geology 24, 1025–1028.

Carbonell, R., Martí, D., Trygvason, A., 1999. Estudios Geológico-Estructurales y Geofísicos en Mina Ratones. Informe Final: Geofísica. Enresa 10-CJA-IF-02.

Cassiraga, F.E., Gómez Hernández, J.J., 1996. Métodos geoestadísticos parala integración de la información. Publicación Técnica de Enresa 04/96, 81pp.

Castro, A., 1986. Structural pattern and ascent model in the Central Extremadura batholith, Hercynian belt, Spain. Journal of Structural Geology 8, 633–645.

Chester, F.M., Logan, J.M., 1986. Implications for mechanical properties of brittle faults from observations of the Punchbowl Fault zone, California. Pure and Applied Geophysics 124 (1/2), 79–106.

Chester, F.M., Logan, J.M., 1987. Composite planar fabric of gouge from the Punchbowl Fault, California. Journal of Structural Geology 9, 621–634.

Chester, F.M., Evans, J.P., Biegel, R.L., 1993. Internal structure and weakening mechanisms of the San Andreas fault. Journal of Geophysical Research 98, 771–786.

Deutsch, C.V., Journel, A.G., 1992. GSLIB Geostatistical Software Library and User's Guide, Oxford University Press, New York, NY.

Díez Balda, M.A., Vegas, R., González Lodeiro, F., 1990. Central-Iberian zone structure. In: Dallmeyer, R.D., Martínez García, E. (Eds.), Pre-Mesozoic Geology of Iberia, Springer-Verlag, Berlin, pp. 172–188.

Engelder, T., Gross, M.R., Pinkerton, P., 1997. Joint development in clastic rocks of the Elk Basin anticline, Montana-Wyoming. In: Hoak, T., Klawitter, A., Blomquist, P. (Eds.), An Analysis of Fracture Spacing versus Bed Thickness in a Basement-involved Laramide Structure, Rocky Mountain Association Geol. 1997 Guidebook, Denver, pp. 1–18.

Englund, E., Sparks, A., 1991. Geo-EAS 1.2.1 User's Guide, EPA Report #600/8-91/008 EPA-EMSL, Las Vegas, NV.

Enresa, 1996. Memoria Cartografía Geológica y Estructural. Rocas Plutónicas, Albalá (G111). Enresa Internal Report (94-G111-IF), Madrid, Vol. II, 249pp.

Escuder Viruete, J., 1999. Estudios Geológico-Estructurales y Geofísicos en Mina Ratones. Informe Final: Estructura. Enresa 10-CJA-IF-01, 134pp.

Escuder Viruete, J., Pérez Estaún, A., 1998. Fracturación en Mina Ratones. Informe Final 1: Estructura, Enresa 10-CJA-IF-01 (Informe de Avance), 33pp.

Escuder Viruete, J., Carbonell, R., Jurado, M.J., Martí, D., Pérez-Estaún, A., 2001. Two-dimensional geostatistical modelling and prediction of the fracturation in the Albala granitic pluton, SW Iberian Massif, Spain. Journal of Structural Geology 23, 2011–2023.

Evans, J.P., Chester, F.M., 1995. Fluid–rock interaction in faults of the San Andreas system: inference from San Gabriel fault-rock geochemistry and microstructures. Journal of Geophysical Research 100, 13007–13020.

Forster, C.B., Evans, J.P., 1991. Hydrogeology of thrust faults and crystalline thrust sheets: results of combined field and modeling studies. Geophysical Research Letters 18, 979–982.

Gil, C., Pérez Rojas, S., 1982. Memoria del MAGNA no. 764 (Albalá). IGME, Madrid.

Goddard, J., Evans, J.P., 1995. Chemical changes and fluid–rock interaction in faults of crystalline thrust sheets, northwestern Wyoming, USA. Journal of Structural Geology 17, 533–547.

Gómez Hernández, J.J., Srivastava, R.M., 1989. ISIM3D: an ANSI-C three-dimensional multiple indicator conditional simulation program. Computer and Geosciences 16, 395–440.

Gómez Hernández, J.J., Cassiraga, F.E., 1994. Theory and practice of sequential simulation. In: Armstrong, M., Dowd, P.A. (Eds.), Geostatistical Simulations, pp. 111–124.

Goovarets, P., 1997. Geostatistics for Natural Resources Evaluation, Oxford University Press.

Gumiel, P., Campos, R., 1993. Contribución al conocimiento geológico y geoquímico de los granitos de Albalá y Montánchez (Extremadura Central) y su relación con las mineralizaciones de estaño y wolframio. Geogaceta 13, 57–61.

Hancock, P.L., 1985. Brittle microtectonics: principles and practice. Journal of Structural Geology 7, 437–457.

Isaaks, E., Srivastava, R.M., 1989. An Introduction to Applied Geostatistics, Oxford University Press.

Journel, A.G., 1989. Fundamentals of geostatistics in five lessons. Short Course in Geology. American Geophysical Union, Vol. 8, 40pp.

Julivert, M., Fontbote, J.M., Ribeiro, A., Conde, L., 1972. Mapa Tectónico de la Península Ibérica y Baleares. E. 1:1 000000. IGME, Madrid.

Jurado, M.J., 1999. Avance sobre la evaluación de la Testificación geofísica de sondeos adquirida en Mina Ratones. Enresa Internal Report 10-CJA-IA-12, 72pp.

Kupfersberger, H., Deutsch, C.V., 1999. Methodology for integrating analog geologic data in 3-D variogram modeling. American Association of Petroleum Geologists 83, 1262–1278.

La Pointe, P.R., Hudson, J.A., 1985. Characterization and interpretation of rock mass joint patterns. Geological Society of America, Special Paper, 199, 37pp.

Little, T.A., 1996. Faulting-related displacement gradients and strain adjacent to the Aware strike-slip fault in New Zealand. Journal of Structural Geology 18, 321–340.

Lopez, D.L., Smith, L., 1996. Fluid flow in fault zones: influence of hydraulic anisotropy and heterogeneity on the fluid flow and heat transfer regime. Water Resources Research 32, 3227–3235.

Martí, D., Carbonell, R., Trygvason, A., Escuder Viruete, J., Perez-Estaun, A., 2002. Mapping brittle fracture zones in 3-dimensions: high resolution travel time seismic tomography in a granitic pluton. Geophysical Journal International 149, 95–105.

Martínez, A., Ramírez, E., 1966. El yacimiento uranífero de Los Ratones, Albalá (Cáceres). Boletín Geológico y Minero 41, 1–28.

Narr, W., Suppe, J., 1991. Joint spacing in sedimentary rocks. Journal of Structural Geology 13, 1037–1048.

Ortega, E., Hernández Urroz, J., González Lodeiro, F., 1988. Distribución paleogeográfica y control estructural de los materiales anteordovícicos en la parte suroriental del autóctono de la Zona Centro Ibérica. II Congreso Español de Geología. Simposios, pp. 85–89.

Pannatier, Y., 1996. VARIOWIN 2.2.: Software for Spatial Data Analysis in 2D, Springer-Verlag, New York, NY.

Pebesma, E.J., Wesseling, C.G., 1998. Gstat, a program for geostatistical modeling, prediction and simulation. Computers and Geosciences 24 (1), 17–31.

Pérez Estaún, A., 1999. Estudios Geológico-Estructurales y Geofísicos en Mina Ratones. Informe Final: Conclusiones. Enresa 10-CJA-IF-03, 30pp.

Pérez Estaún, A., Martínez Catalán, J.R., Bastida, F., 1991. Crustal

thickening and deformation sequence in the footwall to the suture of the Variscan belt of Northwest Spain. Tectonophysics 191, 243–253.

Reguilón, R.M., 1988. Las mineralizaciones de uranio y fósforo de los granitos de Trujillo, Plasenzuela, Albalá, Montánchez y Alburquerque. Ph.D. thesis, Univ. de Salamanca, 276pp.

Reguilón, R., Arribas, A., Martín-Izard, A., Mangas, J., 1996. Las mineralizaciones de U de la Carretona y Casa del Gallo en el granito de Albalá (Cáceres). Geogaceta 20 (7), 1598–1600.

Sanderson, D.J., Roberts, S.P., McGowan, J., Gumiel, P., 1991. Hercynian transpresive tectonics at the southern margin of the Central-Iberian Zone, West Spain. Journal Geological Society of London 148, 893–899.

Scholz, C.H., Anders, M.H., 1994. The permeability of faults. In: The Mechanical Involvement of Fluids in Faulting. U.S. Geological Survey. Open-File Report 94-228, pp. 247–253.

Schulz, S.E., Evans, J.P., 1998. Spatial variability in microscopic deformation and compositions of the Punchbowl fault, southern California: implications for mechanisms, fluid-rock interaction, and fault morphology. Tectonophysics 295, 223–244.

Schulz, S.E., Evans, J.P., 2000. Mesoscopic structure of the Punchbowl Fault, Southern California and the geologic and geophysical structure of active strike-slip faults. Journal of Structural Geology 22, 913–930.

Smith, L., Forster, C.B., Evans, J.P., 1990. Interaction of fault zones, fluid flow and heat transfer at the basin scale. In: Hydrogeology of Low Permeability Environments. International Association of Hydrogeologists 2, pp. 41–67.

Terzaghi, R.D., 1965. Sources of errors in joint surveys. Geotechnique 15, 287–304.